


## Time-dependent first-principles study of angle-resolved secondary electron emission from atomic sheets

Yoshihiro Ueda, Yasumitsu Suzuki, and Kazuyuki Watanabe\*

*Department of Physics, Tokyo University of Science, 1-3 Kagurazaka, Shinjuku-ku, Tokyo 162-8601, Japan* (Received 12 November 2017; revised manuscript received 19 January 2018; published 6 February 2018)

Angle-resolved secondary electron emission (ARSEE) spectra were analyzed for two-dimensional atomic sheets using a time-dependent first-principles simulation of electron scattering. We demonstrate that the calculated ARSEE spectra capture the unoccupied band structure of the atomic sheets. The excitation dynamics that lead to SEE have also been revealed by the time-dependent Kohn-Sham decomposition scheme. In the present study, the mechanism for the experimentally observed ARSEE from atomic sheets is elucidated with respect to both energetics and the dynamical aspects of SEE.

DOI: [10.1103/PhysRevB.97.075406](https://doi.org/10.1103/PhysRevB.97.075406)

### I. INTRODUCTION

The electronic band structure of materials is a prerequisite to understanding fundamental properties in condensed matter physics. Therefore, considerable attention has been paid to probing the band structure experimentally. There are several established experimental methods that can obtain the occupied band structure. Angle-resolved photoemission spectroscopy (ARPES) [1,2] is one of the most widely used methods and is based on the information that photoelectrons provide with respect to the energy and momentum of electrons in a crystal due to the conservation of energy and momentum.

However, probing the unoccupied band structure has been considered more challenging than probing the occupied band structure, so that there have been few methods developed to this end. Among them, very low-energy electron diffraction (VLEED) spectroscopy [3] is a method that can provide the band structure above the vacuum level by measuring the intensity of reflected electrons as a function of electron energy and momentum. Angle-resolved low-energy electron transmission [4], which examines the transmission of electrons through free-standing materials as a function of the energy and probing angle, can also provide the unoccupied band structure.

Angle-resolved secondary electron emission (ARSEE) [5–7] is another experimental method that has the potential to determine the unoccupied band structure. Secondary electrons (SEs) are defined as excited electrons emitted from a target when high-energy electrons are incident on the target. Emission of SEs is considered to consist of three steps: (1) excitation to unoccupied bands in the bulk material, (2) migration from the bulk to the surface, and (3) emission from the surface. In electron scattering that leads to SEE, unlike electron-photon interactions in an ARPES experiment, the incident electrons can transfer their own kinetic energy to the target, and thus electronic excitation to various unoccupied bands can occur. Therefore, it is considered that the SEs from atomic sheets, where there is no bulk migration process, can

provide information on unoccupied bands during emission. Angle-resolved energy spectra of SEs are considered to reflect the unoccupied band structure of materials on the basis of this idea. Recently, Pisarra *et al.* [8] reported an experimental ARSEE spectrum for graphene on a Ni substrate and revealed a close relationship between the ARSEE spectrum and the calculated band structure. Such a relationship between the emitted electrons and the band structure of graphene was also predicted by Nazarov *et al.* [9]. They showed that an electron moving with sufficiently high energy within a layer has the probability to escape into the vacuum by coupling of the in-plane and perpendicular electron motions using an exactly solvable model.

Recently, many studies in fundamental physics and on advanced technological applications have been conducted to explore atomic layered materials due to their novel properties, which are different from those of their bulk counterparts [10–15]. Graphene is a representative layered material because of its perfect two-dimensional structure and exceptional electronic and mechanical properties [16–20]. Silicene, which is a single atomic layer of silicon much like graphene, is also a well studied material with properties similar to those of graphene [21–24]. However, it is well known that there are several differences between graphene and silicene, e.g., silicene has a buckled structure due to weaker  $\pi$  bonding and a small band gap due to stronger spin-orbit interactions. Such characteristics of silicene are of interest with respect to its function as a topological insulator [24]. Considering the electronic and geometric differences between graphene and silicene, it is very important to reveal how these differences affect the mechanism of SEE. Elucidation of the SEE mechanism in atomic sheets will also validate the interpretation of ARSEE and lead to further development of the ARSEE technique.

There have been no theoretical studies that directly calculate the ARSEE spectra from first principles and compare them with the band structure, although several studies [8,9] support the idea that ARSEE spectra can be used to obtain the unoccupied band structure of two-dimensional materials. In this study, we calculate the ARSEE spectra of graphene and silicene using a novel approach developed on the basis of time-dependent

\*kazuyuki@rs.kagu.tus.ac.jp

density functional theory (TDDFT) [25–27]. Recently, Dauth *et al.* [28] reported that TDDFT can be used to reproduce experimentally obtained ARPES maps. De Giovannini *et al.* [29] have also presented a new theoretical approach to simulate spin- and time-resolved ARPES maps based on TDDFT. Here, we demonstrate how TDDFT captures the essential features of ARSEE. We show that the unoccupied band structure, especially that localized in the target, is responsible for the ARSEE spectra. Lastly, we elucidate the detailed dynamical properties of SEE by simulation of the particle-hole excitation upon electron impact within the Kohn-Sham (KS) decomposition scheme.

## II. METHOD AND MODEL

We have recently developed a method based on TDDFT to investigate electron scattering processes [30–32]. In the present study, this method was applied to the calculation of ARSEE from atomic sheets.

Figure 1 shows a schematic diagram of the calculation box. The target graphene or silicene [the primitive cell is shown in Fig. 1(b)] is placed at the center of the box, i.e., at  $z = 0$  on the  $x$ - $y$  plane. The electron wave packet (WP) is shot along the direction perpendicular to the target plane from the positive  $z$  region. Complex absorbing potentials (CAP) [33,34], which are 5.3 Å wide, are placed at both ends of the calculation box and the electrons entering the CAP regions disappear immediately (the details can be found in the Appendix).

The computational procedure is as follows. First, the ground state for the target (graphene or silicene) is determined using density functional theory [35,36]. Next, the extra orbital that corresponds to the incident WP is added to the system, which is expressed as

$$\psi_{\text{WP},\mathbf{k}=\Gamma}(\mathbf{r}) = \left(\frac{1}{\pi\sigma^2}\right)^{\frac{1}{4}} \exp\left[-\frac{(z-z_0)^2}{2\sigma^2} + ik_0(z-z_0)\right], \quad (1)$$

where  $\sigma$ ,  $z_0$ , and  $k_0$  are the initial standard deviation, initial center position, and initial wave vector of the WP, respectively. (Atomic units are adopted for equations throughout the paper, unless stated otherwise. The numerical parameters used in the calculations are given in different units.) A WP that is uniform

in the  $x$ - $y$  plane is used; therefore, the orbital of the WP exists only at the  $\Gamma$  point in  $\mathbf{k}$ -space representation [32]. Finally, the orbitals  $\psi_{i,\mathbf{k}}(\mathbf{r},t)$  that belong to the target and the orbital  $\psi_{\text{WP},\mathbf{k}}(\mathbf{r},t)$  that belongs to the incident WP at  $t = 0$  are evolved in time according to the time-dependent Kohn-Sham (TDKS) equations:

$$i\frac{\partial}{\partial t}\psi_{i,\mathbf{k}}(\mathbf{r},t) = H_{\text{TDKS}}[n(\mathbf{r},t)]\psi_{i,\mathbf{k}}(\mathbf{r},t), \quad (2)$$

$$i\frac{\partial}{\partial t}\psi_{\text{WP},\mathbf{k}}(\mathbf{r},t) = H_{\text{TDKS}}[n(\mathbf{r},t)]\psi_{\text{WP},\mathbf{k}}(\mathbf{r},t), \quad (3)$$

and

$$n(\mathbf{r},t) = \frac{1}{N_{\mathbf{k}}} \sum_{\mathbf{k}} \left[ 2 \sum_{i=1}^{N/2} |\psi_{i,\mathbf{k}}(\mathbf{r},t)|^2 + |\psi_{\text{WP},\mathbf{k}}(\mathbf{r},t)|^2 \right], \quad (4)$$

where  $\mathbf{k}$  is the wave vector,  $i$  runs from 1 to  $N/2$  ( $N = 8$  is the number of valence electrons in the target), and  $N_{\mathbf{k}}$  is the number of sampled  $\mathbf{k}$  points. We note that we used the spin-unpolarized scheme, and a singly occupied  $\psi_{\text{WP}}$  corresponds to an ensemble of incoming spin-up and spin-down electrons. We also note that our approach implies identifying Kohn-Sham particles with electrons.

In this study, the kinetic energy  $E_{\text{kin}} = \mathbf{k}^2/2 = 200$  eV and the width 0.53 Å for the incident WP are used. We chose 200 eV incident energy because it generates a sufficient number of SEs for our analysis both for graphene and silicene and 0.53 Å width that corresponds to 13.6 eV in energy to save the computational cost. The initial distance, 6.35 Å, of the WP from the target plane is sufficiently large to neglect the overlap between the orbitals. A norm-conserving pseudopotential [37,38] and an adiabatic local-density approximation (ALDA) [39] for the exchange-correlation (xc) interaction are used in  $H_{\text{TDKS}}$ . We note that ALDA is not self-interaction free [40] and known to lack important nonadiabatic xc features [41,42], so our results below may lack some features arising from electron-electron interaction such as energy loss due to plasmonlike excitations within the target. We also note that, in this work, the initial state is not a ground state, and thus in principle we have to worry about the initial state dependence of the xc potential. However, as we used ALDA, where the xc potential functional depends only on the instantaneous density, we cannot discuss the initial state dependence here. The number of sampled  $\mathbf{k}$  points is 900, including the  $\Gamma$  point. A time step  $\Delta t = 1.45 \times 10^{-4}$  fs and a cutoff energy of 1.4 keV are used. The atomic positions are fixed during the simulation because the total simulation time is too short to observe atomic motion. We used periodic boundary condition for all directions. In the  $z$  direction, we have checked that the KS potential is flat in space in the vacuum region by the DFT calculation. This means that the interaction between electrons in the different supercells is negligibly small. In TDDFT calculation, however, the KS potential is not flat due to the presence of the WP. Nevertheless, the electron dynamics itself is properly described in the present simulation, since the spacing of the two WPs in the nearest neighbor unit cells is large enough for neglecting the repulsive interaction between them.

The time-dependent orbitals in the electron scattering process are obtained with this procedure, which then allows the

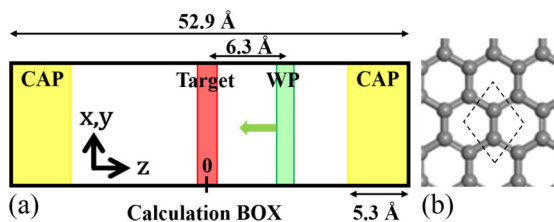


FIG. 1. (a) Schematic diagram of the calculation box. Periodic boundary conditions are used for all directions. The target graphene or silicene is at the center of the box. The initial position of the wave packet (WP) is 6.35 Å away from the target. Complex absorbing potentials (CAP) are placed at both ends. (b) Atomic structure of the target, where the gray balls denote C atoms (graphene) or Si atoms (silicene). For silicene, there is a buckled structure along the  $z$  direction. The dashed line denotes the unit cell used for the calculation.

ARSEE spectra to be calculated by Fourier transformation of the time-dependent orbitals [43],

$$P_{\mathbf{k}}(\omega, z) = \int dx dy \sum_i^{N/2} \left| \int_0^T dt \psi_{i,\mathbf{k}}(\mathbf{r}, t) e^{i\omega t - \Gamma t} \right|^2, \quad (5)$$

at the observation plane of  $z = -17.5 \text{ \AA}$ . This gives the  $\mathbf{k}$ -resolved energy spectra of the SEs. We consider that the  $\mathbf{k}$ -resolved energy spectra are the same as the ARSEE spectra. The experimental results reported in Ref. [8] support this idea.  $T$  and  $\Gamma$  denote the simulation time (2.9 fs) and damping factor (2.1 eV), respectively. We introduce the damping factor to eliminate artificial wiggle structures around the peak energies because of incomplete oscillatory behavior in the finite time region [44].  $i$  runs from 1 to  $N/2$ , and  $\psi_{\text{WP}}$  is not included in the summation to remove the contribution of incident (primary) electrons. Here, the energy  $\omega$  of the peak position in the spectrum  $P_{\mathbf{k}}(\omega, z)$  corresponds to the energy of either bound states or scattering states. The ARSEE is under examination; therefore, the scattering electrons (emitted toward the vacuum) with positive energy must be extracted instead of the bound state electrons in the bulk with negative energies. Thus, the energy zero indicates the vacuum level for electrons in the ground state. However, in the electron scattering state, the KS potential that is experienced by electrons is no longer flat in space and even time dependent, so that the vacuum level is not uniquely defined. In other words, the energy zero does not have a simple physical meaning. In the following, we use the term “the vacuum level” to indicate the vacuum level in the ground state.

The projection of  $\mathbf{k}$ -resolved density of states (DOS) onto the target region (projected  $\mathbf{k}$ -DOS [Pk-DOS]) [8] was also calculated to explore if the band structure above the vacuum level is responsible for the ARSEE spectra. Consider the separation of the DOS into two parts:

$$\begin{aligned} \rho(E) &= 2 \sum_{i,\mathbf{k}} \delta(E - E_{i,\mathbf{k}}) \\ &= 2 \sum_{i,\mathbf{k}} \left( \int_{\text{vacuum}} d\mathbf{r} + \int_{\text{target}} d\mathbf{r} \right) |\psi_{i,\mathbf{k}}(\mathbf{r})|^2 \delta(E - E_{i,\mathbf{k}}), \end{aligned} \quad (6)$$

where  $E_{i,\mathbf{k}}$  is the energy of the  $i$ th level at the  $\mathbf{k}$  point, and the integration regions, “vacuum” and “target” represent  $|z| > 4.0 \text{ \AA}$  and  $|z| \leq 4.0 \text{ \AA}$ , respectively, as in Ref. [8]. Then, Pk-DOS  $\rho_{\mathbf{k}}^p(E)$  is defined as

$$\rho_{\mathbf{k}}^p(E) \equiv \sum_i n_{i,\mathbf{k}}^p \delta(E - E_{i,\mathbf{k}}), \quad (7)$$

$$n_{i,\mathbf{k}}^p \equiv 2 \int_{\text{target}} d\mathbf{r} |\psi_{i,\mathbf{k}}(\mathbf{r})|^2. \quad (8)$$

Thus, the Pk-DOS gives the DOS only of the states that are localized in the target. In the DFT calculation of systems that have a vacuum region in the supercell, the band structure has quasicontinuum states above the vacuum level. By calculating the Pk-DOS, it is possible to distinguish two types of quasicontinuum states; one is localized near the slab and the other is delocalized, i.e., extended into the vacuum.

We calculate the time-dependent electron numbers in levels that belong to the target upon electron impact within the KS decomposition scheme [45],

$$M_{i,\mathbf{k}}(t) = 2 \sum_j^{\text{occ.}} |\langle \psi_{i,\mathbf{k}}(\mathbf{r}, 0) | \psi_{j,\mathbf{k}}(\mathbf{r}, t) \rangle|^2, \quad (9)$$

to explore the particle-hole excitation that leads to SEs. Here,  $i$  runs over all levels obtained in the KS ground state, and  $j$  runs from 1 to  $N/2$  for the occupied ground states and the WP states.

To understand these physical quantities [ARSEE spectra (5), Pk-DOS (7) and the number of electrons in the KS levels (9)] and to clarify the relevance among them, a map of each  $\mathbf{k}$ - and energy-dependent intensity is plotted by calculating

$$I_{\mathbf{k}}^{\text{ARSEE}}(E, z) = \sum_n P_{\mathbf{k}}(E_{n,\mathbf{k}}^{\text{peak}}, z) G_{\sigma}(E - E_{n,\mathbf{k}}^{\text{peak}}), \quad (10)$$

$$I_{\mathbf{k}}^p(E) = \sum_i n_{i,\mathbf{k}}^p G_{\sigma}(E - E_{i,\mathbf{k}}), \quad (11)$$

$$I_{\mathbf{k}}^{\text{KS}}(E, t) = \sum_i M_{i,\mathbf{k}}(t) G_{\sigma}(E - E_{i,\mathbf{k}}), \quad (12)$$

where  $G_{\sigma}$  is a Gaussian function with a standard deviation of  $\sigma = 0.7 \text{ eV}$ , which is used instead of a  $\delta$  function to broaden the peaks [8].  $E_{n,\mathbf{k}}^{\text{peak}}$  denotes the  $n$ th peak energy in the energy spectra  $P_{\mathbf{k}}(\omega, z)$ .

### III. RESULTS AND DISCUSSION

#### A. ARSEE spectra

First, we present the close relationship between the ARSEE [Eq. (10)] and the Pk-DOS [Eq. (11)]. The color maps in Figs. 2(a) and 2(b) show the Pk-DOS for graphene (upper panel) and silicene (lower panel), while Figs. 2(c) and 2(d) show the ARSEE spectra for each system. Colors indicate the intensities as shown by the color bar. The color scales in (a) and (b) are the same, and those in (c) and (d) are the same. The vertical axes indicate the energy measured from the Fermi level, and the horizontal axes indicate the sampling  $\mathbf{k}$  path in the Brillouin zone. The zero values for the energy axes in the ARSEE spectra are set such that the first peak energy at the  $\Gamma$  point in each ARSEE spectrum is aligned with that in the Pk-DOS above the Fermi level. The white lines denote the vacuum levels (4.6 eV for graphene and 4.8 eV for silicene). Black dots in these figures indicate the band structure for the ground state. The Pk-DOS below the Fermi level is almost the same as the  $\mathbf{k}$ -DOS (not shown here) because  $\psi_{i,\mathbf{k}}(\mathbf{r})$  is localized in graphene and  $n_{i,\mathbf{k}}^p$  is almost two.

We note the four main peaks in Figs. 2(a) and 2(c) by focusing on the  $\Gamma$  point (indicated by red circles). The peaks in Fig. 2(a) correspond to the 5th, 22nd (23rd), 29th, and 33rd bands from the bottom of the band on the  $\Gamma$  point. These are more apparent in Fig. 2(e), which gives the intensities of Pk-DOS (dashed curve) and ARSEE (solid curve) on the  $\Gamma$  points and shows the common properties between them. The three peaks in the negative energy region of (e) (dashed curve) are the four occupied bands, where the highest one is degenerate, as shown in Figs. 2(a) and 2(c). We can compare the



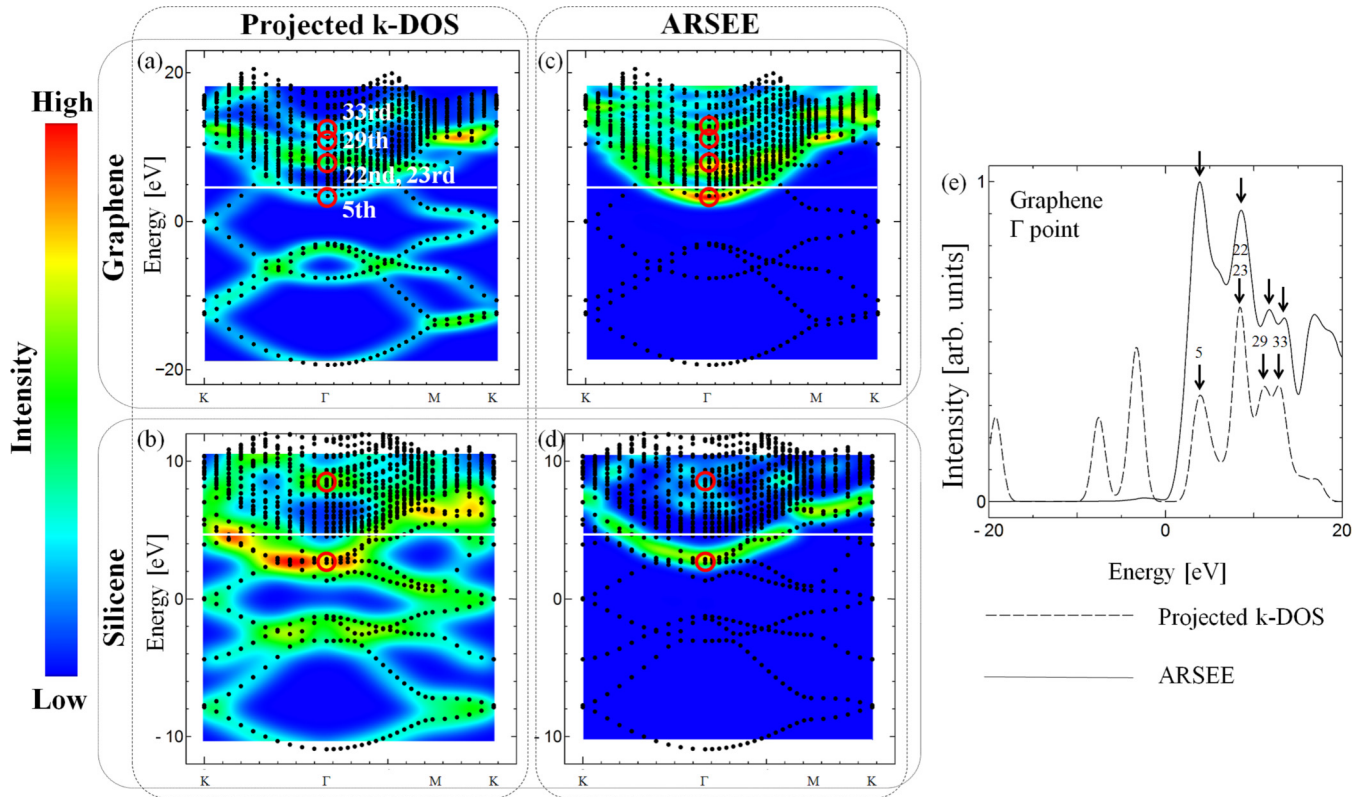


FIG. 2. Pk-DOS for (a) graphene and (b) silicene. Calculated ARSEE spectra for (c) graphene and (d) silicene. (e) Energy spectra of Pk-DOS (dashed line) and ARSEE (solid line) for graphene at the  $\Gamma$  point. The arrows indicate the positions of four main peaks shown by the red circles in (a) and (c).

energy spacings of the four peaks in the positive energy region between the ARSEE spectrum and Pk-DOS. These four peaks in the Pk-DOS, by definition, correspond to the unoccupied states that are localized in the target. Their spacings are 4.8, 3.2, and 1.4 eV, and the spacings in the ARSEE spectrum are 4.8, 3.2, and 2.1 eV, thereby showing good agreement between them. We also checked initial WP energy dependence of the ARSEE spectra and found that the peak heights of the energy spectra change but the peak positions do not by changing the initial WP energy.

The present results enable us to conclude that at least within the ALDA, the ARSEE spectrum reflects the Pk-DOS for the unoccupied states. This validates the following mechanism for SEE: Upon electron impact, electrons in the target are excited to localized unoccupied states from which electrons are emitted. We note that there are some differences between the ARSEE spectrum and Pk-DOS, e.g., while the ARSEE spectrum shows only downward parabolas, the Pk-DOS has other structures. As mentioned in Sec. II, we considered that the calculated  $\mathbf{k}$ -resolved energy spectra are the same as the ARSEE spectra. However, our results are not in satisfactory agreement with the Pk-DOS, which might indicate the quantitative difference between the angle-resolved and  $\mathbf{k}$ -resolved energy spectra. The reason could be the special shape of the WP, which is uniform in the  $x$ - $y$  plane and has only  $\Gamma$  point symmetry in the  $\mathbf{k}$ -space representation. This issue should be clarified by further calculating different model systems, e.g., using a projectile of 3D WP instead of 1D WP in the next study.

The properties found for graphene are also observed for silicene [Figs. 2(b) and 2(d)]. Qualitative differences in the intensities (color maps) and energy bands (black dots) between graphene (upper) and silicene (lower) are due to the differences in the intrinsic electronic structure between graphene and silicene. Otherwise, the close relationship between Pk-DOS and ARSEE also holds for silicene; the spacings of the first and second peaks (red circles in the lower panels) are 5.6 eV for Pk-DOS and 5.7 eV for ARSEE.

## B. Time- and $\mathbf{k}$ -resolved electron excitation

We have shown the close relationship between the Pk-DOS and ARSEE in the previous section. Here, we study the dynamical process of SEE that governs the basic properties of ARSEE. Electron-impact induced particle-hole excitation dynamics, which is followed by SEE, is described properly with the Kohn-Sham decomposition scheme [Eq. (12)].

Figures 3(a)–3(c) (upper panels) show the  $I_{\mathbf{k}}^{\text{KS}}(E, t)$  at  $t = 0$  fs,  $t = 0.1$  fs (just after electron impact) and  $t = 2.4$  fs (after SEE), respectively, for electron impact with an energy of 200 eV. The colors represent the number of electrons (or occupation number) for each level, as indicated by the same color bar shown in Fig. 2. The numbers of electrons in the excited states above the Fermi level are multiplied by 10 for clarity because the numbers are much smaller than those for the occupied states below the Fermi level. The number of excited electrons is 0.87 (the number of valence electrons in the target is 8) in the unit cell at the  $\Gamma$  point. The profile below the Fermi

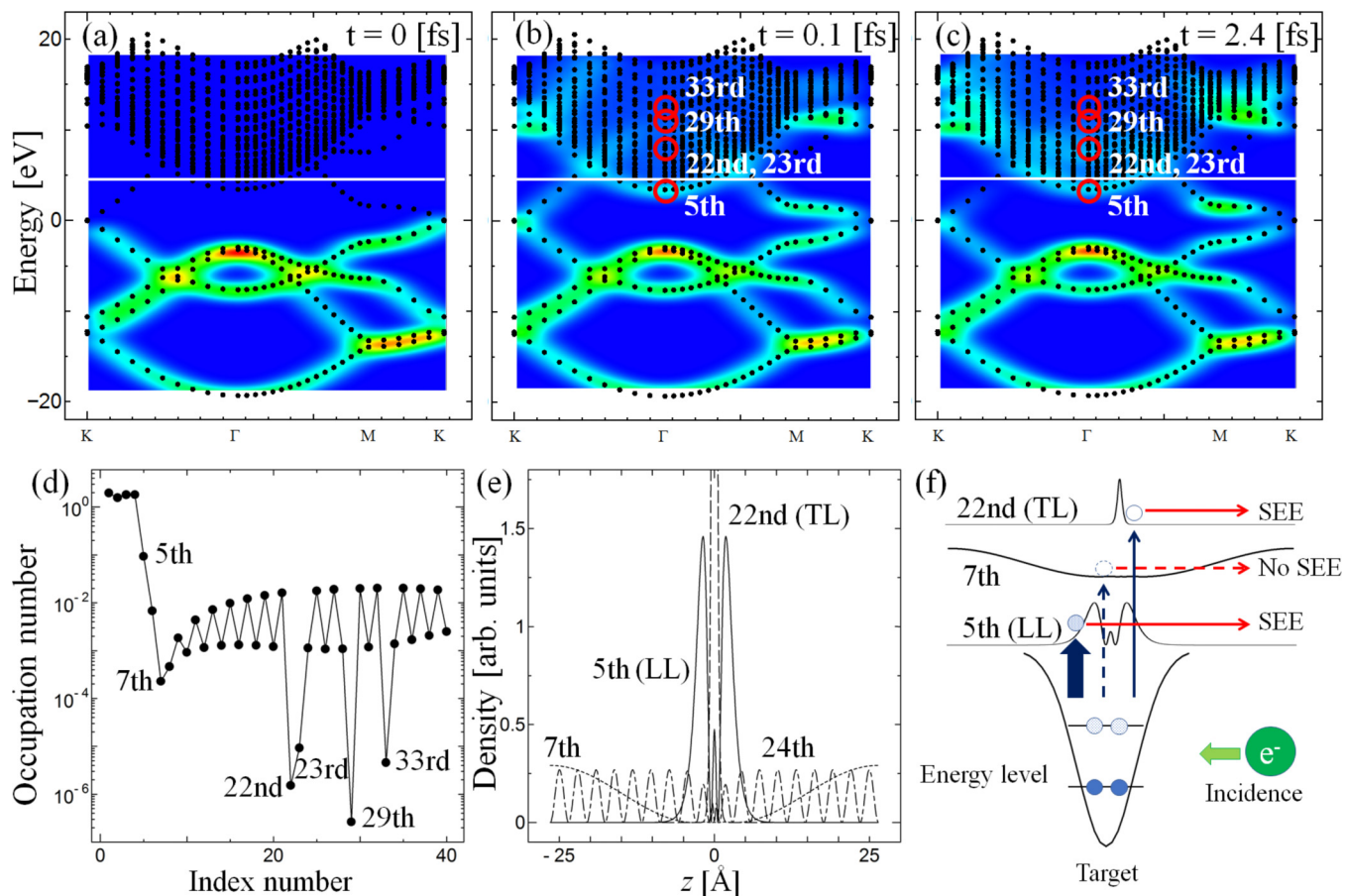


FIG. 3. (a)–(c) Snapshots of the time evolution of the occupation number for KS levels [Eq. (12)] for graphene [(a)  $t = 0$  fs, (b)  $t = 0.1$  fs (just after electron impact), and (c)  $t = 2.4$  fs (after SEE)]. (d) Occupation number at the  $\Gamma$  point at  $t = 0.1$  fs. (e) State densities in the ground state  $n_{i,k=\Gamma}(z) = \int dx dy |\psi_{i,\Gamma}(\mathbf{r}, t = 0)|^2$ . (f) Schematic diagram for SEE from graphene.

level (energy zero) in Fig. 3(a) is essentially the same as that for  $\mathbf{k}$ -DOS in Fig. 2(a). The black dots denote the band structure of graphene in the ground state, as in Figs. 2(a) and 2(c).

Several features worthy of discussion can be identified in Figs. 3(b) and 3(c). The occupation numbers start to decrease below the Fermi level, and increase just above the Fermi level and below the vacuum level (white line), as shown in Fig. 3(b). This demonstrates particle-hole excitation caused by high-energy electron impact. The numbers at the levels around 10 eV further increase (slightly, because they are multiplied by 10), which indicates excitation to higher energy levels with time. More interestingly, the two upward and downward parabolic curves around the vacuum level in Fig. 3(b) match the two parabolas among the bright curves around the vacuum level in Fig. 2(a). This is an important signature of the present excitation, i.e., the excited states that get occupied after electron impact above the Fermi level have a large state-density amplitude around the target because the bright curves in Fig. 2(a) were obtained by projecting the states onto the target region. It should also be noted that the color strength and distribution changes very little from Figs. 3(b) to 3(c). This is because the yield of SEs, which is reflected in the change in the numbers between Figs. 3(b) and 3(c), is very small ( $\sim 0.1$  SE to a primary electron) and the SEs are finally absorbed and disappear in the CAP. Therefore, the SEE dynamics cannot be clearly observed in the excitation dynamics of Figs. 3(b)

and 3(c). The signature of the high peak values observed in Fig. 2(c) are not observed in Figs. 3(b) and 3(c). Nevertheless, it provides the nature of the unoccupied states near and above the vacuum level in the target region, to which electrons are excited and from which the excited electrons are emitted as SEs, as described below.

Figure 3(d) shows the occupation number for energy levels at the  $\Gamma$  point at  $t = 0.1$  fs [transformed to a logarithmic scale using the data from (b)]. Having clarified that the states that are responsible for SEE are the 5th, 22nd (23rd), 29th, and 33rd states from Figs. 2(a) and 2(c), these state numbers are given to the levels in Fig. 3(d). The occupation of  $\sim 0.1$  at the 5th level also appears clearly in Fig. 3(b). On the other hand, the occupation numbers for the other levels above the vacuum level are too small to be observed in Fig. 3(b). However, a common property among these emitting levels is evident. The state densities for graphene at the  $\Gamma$  point integrated over the  $x$ - $y$  plane  $n_{i,k=\Gamma}(z) = \int dx dy |\psi_{i,\Gamma}(\mathbf{r}, t = 0)|^2$  are shown in Fig. 3(e). The state densities for these emitting levels are localized at or around the target. (Those of the 23rd, 29th, and 33rd states are not shown in the figure.) To be more precise, the state density for the 5th level is loosely localized (LL) and that for the 22nd level is tightly localized (TL), as shown in Fig. 3(e). The 7th and 24th states, which are not emitting levels, as is evident from Figs. 2(a) and 2(c), are extended through the entire vacuum region [46]. The feature thus appears

contradictory to intuition, because Fig. 3(e) indicates that the localized states are favorable for emission. However, as mentioned in the Introduction, Nazarov *et al.* [9] demonstrated the presence of the “resonant state” in 2D crystals, which originates from the coupling of the in-plane and perpendicular motions. An electron in this resonant state moves with a sufficiently high energy within the layer and parallel to it and has a nonzero probability to escape into vacuum. Here, we consider that the TL states correspond to these resonant states in Ref. [9], because the TL states are also two dimensional and exist above the vacuum level. Therefore, the electrons excited to these TL states have a probability to escape into vacuum, i.e., are emitted as SEs. The fact that our calculation results of ARSEE spectra capture the band structures of the TL states supports this idea to identify our TL states with the resonant states in Ref. [9].

For these reasons, we can interpret the origin of the peaks in Fig. 2(c) qualitatively using the excitation probability [Figs. 3(a)–3(d)] and the orbital distribution [Fig. 3(e)], as follows. The probability of excitation to the 5th level (LL state) is high because this level is close to the valence band maximum (VBM), whereas the emission probability is low because the level is just below the vacuum level. Conversely, the probabilities of excitation to the 22th, (23th), 29th, and 33rd levels (TL states) are low because these are high above the VBM, whereas the emission probabilities are high because of the coupling of the TL states to the perpendicular motion. As a result, the intensities of the two types of ARSEE peaks in Fig. 2(c), which correspond to the LL and TL states, become the same order of magnitude. A schematic of the mechanism for SEE is given in Fig. 3(f). SEE occurs through the unoccupied states near or above the vacuum level localized around (5th) and at (e.g., 22th) the target graphene, but not through the unoccupied states that are extended to (e.g., 7th) the vacuum region.

#### IV. CONCLUSION

The ARSEE spectra of graphene and silicene were determined using real-time TDDFT simulations and the major peaks of the ARSEE spectra were found to reflect those of **Pk-DOS**, which are intrinsic to the unoccupied electronic band structure of the target materials. Therefore, the present study validates the experimental use of ARSEE spectra to probe the unoccupied states of various atomic sheets. This study enables

us to emphasize the important role of TDDFT in the study of time-resolved and **k**-resolved electron emission spectroscopy by not only light irradiation (ARPES) but also electron impact (ARSEE).

#### ACKNOWLEDGMENTS

The authors wish to thank Y. Homma for valuable discussions regarding SEE. K.W. was supported by JSPS KAKENHI Grant No. JP16K05483. Y.S. was supported by JSPS KAKENHI Grant No. JP16K17768. Numerical calculations were performed on the supercomputers at the Institute for Solid State Physics, University of Tokyo.

#### APPENDIX: COMPLEX ABSORBING POTENTIAL

We used a complex absorbing potential (CAP) [33,34] to avoid reentering of scattered or emitted electrons. We checked the absorption efficiency of several CAPs for the wave packet in the vacuum. The efficiency is defined as

$$A = 1 - \frac{\int dt j(z_b, t)}{\int dt j(z_f, t)}, \quad (\text{A1})$$

where  $j(z, t)$  is the current integrated over the  $x$ - $y$  plane,  $z_f$  and  $z_b$  are the positions of the front and back of the CAP. We searched for the best function and parameters of the CAPs such that the efficiency is the highest. The CAP used in the present calculations is given in Eqs. (1) and (11) in Ref. [34]. We optimized their CAP to deal with the high energy incident electrons, and it is expressed as

$$V_{\text{CAP}}(z) = -i \frac{1}{2|z - z_{\text{end}}|} \left( \frac{2\pi}{\Delta z} \right)^2 y(z), \quad (\text{A2})$$

$$\Delta z = |z_{\text{start}} - z_{\text{end}}|, \quad (\text{A3})$$

$$y(z) = \frac{4}{c^2} \left[ \left( 1 - \frac{|z_{\text{start}} - z|}{\Delta z} \right)^{-2} + \left( 1 + \frac{|z_{\text{start}} - z|}{\Delta z} \right)^{-2} - 2 \right], \quad (\text{A4})$$

where  $c$  is a constant 2.62, and  $z_{\text{start}}$  and  $z_{\text{end}}$  are  $\pm 21.2 \text{ \AA}$  and  $\pm 26.5 \text{ \AA}$ , respectively. The absorption efficiency of the CAP for 200 eV wave packet is larger than 99.9%.

- 
- [1] N. V. Smith, M. M. Traum, and F. D. Salvo, *Solid State Commun.* **15**, 211 (1974).  
 [2] A. Damascelli, *Phys. Scr.* **T109**, 61 (2004).  
 [3] V. N. Strocov, R. Claessen, G. Nicolay, S. Hüfner, A. Kimura, A. Harasawa, S. Shin, A. Kakizaki, H. I. Starnberg, P. O. Nilsson, and P. Blaha, *Phys. Rev. B* **63**, 205108 (2001).  
 [4] F. Wicki, J.-N. Longchamp, T. Latychevskaia, C. Escher, and H.-W. Fink, *Phys. Rev. B* **94**, 075424 (2016).  
 [5] R. F. Willis, B. Fitton, and G. S. Painter, *Phys. Rev. B* **9**, 1926 (1974).  
 [6] F. Maeda, T. Takahashi, H. Ohsawa, S. Suzuki, and H. Suematsu, *Phys. Rev. B* **37**, 4482 (1988).  
 [7] M. Bovet, V. N. Strocov, F. Clerc, C. Koitzsch, D. Naumović, and P. Aebi, *Phys. Rev. Lett.* **93**, 107601 (2004).  
 [8] M. Pisarra, P. Riccardi, A. Sindona, A. Cupolillo, N. Ligato, C. Giallombardo, and L. Caputi, *Carbon* **77**, 796 (2014).  
 [9] V. U. Nazarov, E. E. Krasovskii, and V. M. Silkin, *Phys. Rev. B* **87**, 041405 (2013).  
 [10] G. R. Bhimanapati, Z. Lin, V. Meunier, Y. Jung, J. Cha, S. Das, D. Xiao, Y. Son, M. S. Strano, V. R. Cooper, L. Liang, S. G. Louie, E. Ringe, W. Zhou, S. S. Kim, R. R. Naik, B. G. Sumpter, H. Terrones, F. Xia, Y. Wang, J. Zhu, D. Akinwande, N. Alem, J. A. Schuller, R. E. Schaak, M. Terrones, and J. A. Robinson, *ACS Nano* **9**, 11509 (2015).



- [11] S. Balendhran, S. Walia, H. Nili, S. Sriram, and M. Bhaskaran, *Small* **11**, 640 (2015).
- [12] P. Solis-Fernandez, M. Bissett, and H. Ago, *Chem. Soc. Rev.* **46**, 4572 (2017).
- [13] S. Z. Butler, S. M. Hollen, L. Cao, Y. Cui, J. A. Gupta, H. R. Gutierrez, T. F. Heinz, S. S. Hong, J. Huang, A. F. Ismach, E. Johnston-Halperin, M. Kuno, V. V. Plashnitsa, R. D. Robinson, R. S. Ruoff, S. Salahuddin, J. Shan, L. Shi, M. G. Spencer, M. Terrones, W. Windl, and J. E. Goldberger, *ACS Nano* **7**, 2898 (2013).
- [14] Y. Zhang, A. Rubio, and G. L. Lay, *J. Phys. D: Appl. Phys.* **50**, 053004 (2017).
- [15] X. Zhang and Y. Xie, *Chem. Soc. Rev.* **42**, 8187 (2013).
- [16] J. Phiri, P. Gane, and T. C. Maloney, *Mater. Sci. Eng. B* **215**, 9 (2017).
- [17] Y. Zhong, Z. Zhen, and H. Zhu, *FlatChem* **4**, 20 (2017).
- [18] X. Li, L. Tao, Z. Chen, H. Fang, X. Li, X. Wang, J.-B. Xu, and H. Zhu, *Appl. Phys. Rev.* **4**, 021306 (2017).
- [19] A. C. Ferrari, F. Bonaccorso, V. Fal'ko, K. S. Novoselov, S. Roche, P. Boggild, S. Borini, F. H. L. Koppens, V. Palermo, N. Pugno, J. A. Garrido, R. Sordan, A. Bianco, L. Ballerini, M. Prato, E. Lidorikis, J. Kivioja, C. Marinelli, T. Ryhanen, A. Morpurgo, J. N. Coleman, V. Nicolosi, L. Colombo, A. Fert, M. Garcia-Hernandez, A. Bachtold, G. F. Schneider, F. Guinea, C. Dekker, M. Barbone, Z. Sun, C. Galiotis, A. N. Grigorenko, G. Konstantatos, A. Kis, M. Katsnelson, L. Vandersypen, A. Loiseau, V. Morandi, D. Neumaier, E. Treossi, V. Pellegrini, M. Polini, A. Tredicucci, G. M. Williams, B. Hee Hong, J.-H. Ahn, J. Min Kim, H. Zirath, B. J. van Wees, H. van der Zant, L. Occhipinti, A. Di Matteo, I. A. Kinloch, T. Seyller, E. Quesnel, X. Feng, K. Teo, N. Rupesinghe, P. Hakonen, S. R. T. Neil, Q. Tannock, T. Lofwander, and J. Kinaret, *Nanoscale* **7**, 4598 (2015).
- [20] H. Sahin, O. Leenaerts, S. K. Singh, and F. M. Peeters, *Wiley Interdiscip. Rev. Comput. Mol. Sci.* **5**, 255 (2015).
- [21] A. Kara, H. Enriquez, A. P. Seitsonen, L. L. Y. Voon, S. Vizzini, B. Aufray, and H. Oughaddou, *Surf. Sci. Rep.* **67**, 1 (2012).
- [22] A. Dimoulas, *Microelectron. Eng.* **131**, 68 (2015).
- [23] N. J. Roome and J. D. Carey, *ACS Appl. Mater. Interfaces* **6**, 7743 (2014).
- [24] L. C. L. Y. Voon, in *Silicene Structure, Properties and Applications*, edited by M. J. Spencer and T. Morishita (Springer International Publishing, Cham, Switzerland, 2016), pp. 3–33.
- [25] E. Runge and E. K. U. Gross, *Phys. Rev. Lett.* **52**, 997 (1984).
- [26] K. Burke, J. Werschnik, and E. K. U. Gross, *J. Chem. Phys.* **123**, 062206 (2005).
- [27] C. A. Ullrich, *Time-Dependent Density-Functional Theory Concepts and Applications* (Oxford University Press, New York, 2011).
- [28] M. Dauth, M. Graus, I. Schelter, M. Wießner, A. Schöll, F. Reinert, and S. Kümmel, *Phys. Rev. Lett.* **117**, 183001 (2016).
- [29] U. De Giovannini, H. Hubener, and A. Rubio, *J. Chem. Theor. Comput.* **13**, 265 (2016).
- [30] K. Tsubonoya, C. Hu, and K. Watanabe, *Phys. Rev. B* **90**, 035416 (2014).
- [31] Y. Ueda, Y. Suzuki, and K. Watanabe, *Phys. Rev. B* **94**, 035403 (2016).
- [32] H. Miyauchi, Y. Ueda, Y. Suzuki, and K. Watanabe, *Phys. Rev. B* **95**, 125425 (2017).
- [33] D. E. Manolopoulos, *J. Chem. Phys.* **117**, 9552 (2002).
- [34] T. Gonzalez-Lezana, E. J. Rackham, and D. E. Manolopoulos, *J. Chem. Phys.* **120**, 2247 (2004).
- [35] P. Hohenberg and W. Kohn, *Phys. Rev.* **136**, B864 (1964).
- [36] W. Kohn and L. J. Sham, *Phys. Rev.* **140**, A1133 (1965).
- [37] N. Troullier and J. L. Martins, *Phys. Rev. B* **43**, 1993 (1991).
- [38] K. Kobayashi, *Comput. Mater. Sci.* **14**, 72 (1999).
- [39] J. P. Perdew and A. Zunger, *Phys. Rev. B* **23**, 5048 (1981).
- [40] D. Hofmann, T. Körzdörfer, and S. Kümmel, *Phys. Rev. Lett.* **108**, 146401 (2012).
- [41] N. T. Maitra, *J. Chem. Phys.* **144**, 220901 (2016).
- [42] Y. Suzuki, L. Lacombe, K. Watanabe, and N. T. Maitra, *Phys. Rev. Lett.* **119**, 263401 (2017).
- [43] M. Dauth and S. Kümmel, *Phys. Rev. A* **93**, 022502 (2016).
- [44] K. Yabana, T. Nakatsukasa, J.-I. Iwata, and G. F. Bertsch, *Phys. Stat. Sol. (b)* **243**, 1121 (2006).
- [45] T. Otobe, M. Yamagiwa, J.-I. Iwata, K. Yabana, T. Nakatsukasa, and G. F. Bertsch, *Phys. Rev. B* **77**, 165104 (2008).
- [46] The sixth state is also an LL state. All the other states shown in Fig. 3(d) are extended states.